Nanoscale

PAPER

View Article Online
View Journal | View Issue

Cite this: *Nanoscale*, 2024, **16**, 8650

Exploring the potential of CuCoFeTe@CuCoTe yolk-shelled microrods in supercapacitor applications†

Dorsa Dehghanpour Farashah,[a] Maliheh Abdollahi,‡[b] Akbar Mohammadi Zardkhoshoui*[a] and Saied Saeed Hosseiny Davarani *[a]

Driven by their excellent conductivity and redox properties, metal tellurides (MTes) are increasingly capturing the spotlight across various fields. These properties position MTes as favorable materials for next-generation electrochemical devices. Herein, we introduce a novel, self-sustained approach to creating a yolk-shelled electrode material. Our process begins with a metal–organic framework, specifically a CoFe-layered double hydroxide-zeolitic imidazolate framework67 (ZIF67) yolk-shelled structure (CFLDH–ZIF67). This structure is synthesized in a single step and transformed into CuCoLDH nanocages. The resulting CuCoFeLDH–CuCoLDH yolk-shelled microrods (CCFLDH–CCLDHYSMRs) are formed through an ion-exchange reaction. These are then converted into CuCoFeTe–CuCoTe yolk-shelled microrods (CCFT–CCTYSMRs) by a tellurization reaction. Benefiting from their structural and compositional advantages, the CCFT–CCTYSMR electrode demonstrates superior performance. It exhibits a fabulous capacity of 1512 C g^{-1} and maintains an impressive 84.45% capacity retention at 45 A g^{-1}. Additionally, it shows a remarkable capacity retention of 91.86% after 10 000 cycles. A significant achievement of this research is the development of an activated carbon (AC)||CCFT–CCTYSMR hybrid supercapacitor. This supercapacitor achieves a good energy density (E_{den}) of 63.46 W h kg^{-1} at a power density (P_{den}) of 803.80 W kg^{-1} and retains 88.95% of its capacity after 10 000 cycles. These results highlight the potential of telluride-based materials in advanced energy storage applications, marking a step forward in the development of high-energy, long-life hybrid supercapacitors.

Received 6th January 2024,
Accepted 8th April 2024

DOI: 10.1039/d4nr00076e

rsc.li/nanoscale

1. Introduction

In the face of mounting economic progress, the dual challenges of fuel scarcity and environmental pollution necessitate a balance between resource demands and environmental protection. This urgency underscores the importance of research and development in green and sustainable energy. A crucial aspect in the utilization of renewable energies, such as wind, tidal, and solar power, involves their effective storage and conversion.[1–4] Supercapacitors, emerging as a novel class of green energy devices offer numerous advantages. They boast high-power density, outstanding cycle lifespan, rapid charging and discharging capabilities, high specific capacity, safety, absence of memory effect, ease of maintenance, and reliability.[5–11] These attributes make them ideal for utilization in portable electronics, electric-powered vehicles, and wearable devices.[12,13] Nevertheless, the relatively weak E_{den} of supercapacitors, compared to batteries, significantly limits their further advancement.[14,15]

Hybrid supercapacitors offer a promising solution by combining the battery-type (energy source) material with a capacitor-type (power source) material. They typically exhibit higher energy densities than traditional capacitors and greater power densities than conventional batteries.[16–18] The material plays a decisive role in optimizing these hybrid supercapacitors. Recent years have seen considerable efforts in designing novel battery-type electrode materials, focusing on unique structures, morphologies, and chemical compositions.[19–21]

Historically, metal oxides and hydroxides, with their diverse structures and morphologies, have been the primary materials for hybrid supercapacitors.[22,23] These materials often suffer from poor rate capabilities and limited stability due to low

[a]*Department of Chemistry, Shahid Beheshti University, G. C., 1983963113, Evin, Tehran, Iran. E-mail: ss-hosseiny@sbu.ac.ir, mohammadi.bahadoran@gmail.com; Fax: +9821 22431661; Tel: +98 21 22431661*

[b]*Department of Chemistry, University of Isfahan, Isfahan, Iran*

†Electronic supplementary information (ESI) available: Supplementary characterization and electrochemical data, and a benchmark table to compare the performance of as-prepared device with previous reported. See DOI: **https://doi.org/10.1039/d4nr00076e**

‡Current address: Department of Environmental Microbiology, UFZ-Helmholtz Centre for Environmental Research, Leipzig, Germany.

electrical conductivity.[24,25] This limitation necessitates the exploration of electrode materials with superior electrical conductivity for enhanced electrochemical properties. Recently, metal tellurides have emerged as a promising class of materials.[16,17] They offer high electronic conductivity, diverse valences, and remarkable electrochemical activities, making them suitable for supercapacitors, batteries, and even catalysts.[26–28] Bimetal tellurides show enhanced electrochemical activity due to richer redox reactions and faster electronic conduction.[27,28] Furthermore, trimetal tellurides are anticipated to exhibit even better electrical conductivity and performance due to their synergistic effects and more flexible structures.[17]

Iron (Fe)-based materials have gained attention for supercapacitors thanks to their abundant availability and rich redox chemistry.[29] However, their poor conductivity limits their performance. To address this, integrating Fe with other elements such as Cu and Co has been explored, which enhances conductivity and overall electrochemical performance.[30] Additionally, designing yolk-shelled nanostructures has been identified as an effective approach to improving supercapacitive performance.[31] These unique structures, comprising a movable core within a hollow cavity surrounded by a porous shell, are not just at the forefront of material science but also show potential in catalysis, energy storage, and biomedicine.[31–33] Our research group has successfully created $NiCo_2Se_4$ yolk–shell structures with impressive electrochemical properties.[6] Similarly, Xu *et al.* developed yolk–shell $NiSe_2$@C nanocomposites exhibiting excellent electrochemical performance.[34]

The template-engaged synthesis approach has demonstrated its effectiveness in creating diverse hollow micro-/nanostructures, utilizing metal–organic frameworks (MOFs) as self-engaged precursors.[35,36]

In this study, we introduce hierarchical CuCoFeTe–CuCoTe yolk-shelled microrods (CCFT–CCTYSMRs) as electrodes for hybrid supercapacitors. The CCFT–CCTYSMR-based electrode's exceptional performance can be related to the synergy between the metals, the conductivity of tellurium, and the yolk–shell structure. The CCFT–CCTYSMR displayed a capacity of 1512 C g^{-1}, significantly surpassing the CCFLDH–CCLDHYSMR electrode (812 C g^{-1}), and demonstrated fantastic rate capability and durability. Consequently, we assembled the AC||CCFT–CCTYSMR device, achieving an E_{den} of 63.46 W h kg^{-1} at 803.80 W kg^{-1}.

2. Experimental section

2.1. Reagents

In this study, we utilized various reagents including fumaric acid ($C_4H_4O_4$), iron(III) nitrate nonahydrate ($Fe(NO_3)_3{\cdot}9H_2O$), ethanol (C_2H_5OH), methanol (CH_3OH), polyvinylpyrrolidone (PVP, K30, MW~40 000), cobalt nitrate hexahydrate ($Co(NO_3)_2{\cdot}6H_2O$), tellurium powder, 2-methylimidazole ($C_4H_6N_2$), and copper(II) chloride dihydrate ($CuCl_2{\cdot}2H_2O$).

2.2. Synthesis of MIL-88A

Initially, 139.3 mg of $C_4H_4O_4$ was added in 25 mL of H_2O and stirred mechanically at 70 °C for 10 minutes. Subsequently, 525.2 mg of $Fe(NO_3)_3{\cdot}9H_2O$ was added to the mixture and stirred for 20 minutes at the same temperature. Then, the orange mixture was poured into an autoclave and heated at 110 °C for 6 hours. The resulting orange MIL-88A precipitate was obtained through centrifugation and repeatedly washed with C_2H_5OH and H_2O.

2.3. Synthesis of modified MIL-88A

61.5 mg of MIL-88A was mixed in 10 mL of CH_3OH containing 0.5 g PVP. This solution was stirred for 12 hours, after which the modified MIL-88A was collected *via* centrifugation, washed with CH_3OH, and re-dispersed in 5 mL of CH_3OH.

2.4. Synthesis of CFLDH–ZIF67YSMRs

17.46 mg of $Co(NO_3)_2{\cdot}6H_2O$ was added to 3 mL of C_2H_5OH (solution A). Separately, 0.328 g of $C_4H_6N_2$ was added to 5 mL of CH_3OH (solution B). Modified MIL-88A dispersion (0.4 mL) was mixed with 0.6 mL CH_3OH, added to solution A, and ultrasonicated for 1 minute. Solution B was then introduced, and the mixture was heated at 97 °C for 2 hours. The sample was gathered by centrifugation, washed with C_2H_5OH, and dried.

2.5. Synthesis of CCFLDH–CCLDHYSMRs

17.05 mg of $CuCl_2{\cdot}2H_2O$ was added to 40 mL of H_2O and heated at 92 °C for 10 minutes. Subsequently, 1 mL of CH_3OH containing 10 mg of CFLDH@ZIF67 YSMRs was quickly added, and the mixture was heated for 5 minutes. The CCFLDH–CCLDHYSMR sample was obtained through centrifugation and then washed with C_2H_5OH.

2.6. Synthesis of CCFT–CCTYSMRs

20 mg of Te powder and 10 mg of CCFLDH–CCLDHYSMR sample were positioned in separate areas of the porcelain boat within the tube furnace, with the Te powder upstream. The samples were annealed at 600 °C for 2 hours at a heating rate of 2 °C min^{-1} under a nitrogen atmosphere. The CCFT–CCTYSMRs were obtained after cooling in a similar atmosphere.

2.7. Characterizations

The structural and chemical composition of our samples were characterized using a field-emission scanning electron microscope (FESEM MIRA 3 TESCAN, 15 kV, Czech) with an energy dispersive X-ray spectroscopy (EDX) attachment, and a transmission electron microscope (TEM Philips CM200 instrument). X-ray photoelectron spectroscopy (XPS Thermo Scientific: ESCALAB 250Xi Mg X-ray source) was applied to examine the chemical states of the CCFT–CCTYSMR. The crystal phase was analyzed *via* X-ray diffraction (XRD Philips X'Pert Pro X-ray diffractometer). The porosity characteristics of the CCFT–CCTYSMR and CCFLDH–CCLDHYSMR were obtained by N_2 adsorption/desorption studies on the

SSA-4300, with specific surface areas (SSAs) and pore size distributions calculated *via* the Brunauer–Emmett–Teller (BET) and Barrett–Joyner–Halenda (BJH) methods, respectively.

2.8. Electrochemical tests

2.8.1. Three-electrode cell. Our electrodes were prepared through the slurry coating strategy. The slurry, comprising acetylene black, poly(tetrafluoroethylene), and the material in a 1 : 1 : 8 mass ratio in C_2H_5OH, was spread onto a nickel foam (NF). After drying and pressing at 10 MPa, the material mass loading on the electrode was determined by weight comparison of the NF before and after coating, typically around 4 mg. The electrochemical tests of our electrodes were examined in 6.0 M KOH using a three-electrode setup, employing the Hg/HgO electrode as the reference electrode and a Pt foil as the counter electrode. To ensure the reliability of our findings, each electrochemical measurement was conducted in triplicate. The electrode capacity, measured in C g^{-1}, was calculated from the GCD curve *via* the formula $C = I \times \Delta t/m$, where m (g), Δt (s), and I (A) manifest the mass of our samples, discharge time, and current. The coulombic efficiency (CE) of CCFT–CCTYSMR and AC||CCFT–CCTYSMR was determined *via* CE = T_D/T_C, where T_D(sec) and T_C(sec) show the discharging and charging times, respectively.

2.8.2. Fabrication of the AC||CCFT–CCTYSMR. To assess the actual utilization of the CCFT–CCTYSMR, we fabricated a hybrid device (AC||CCFT–CCTYSMR). The CCFT–CCTYSMR and AC were first soaked in KOH to optimize electrolyte absorption. Separation was achieved using a cellulose paper separator, and the assembly of AC||CCFT–CCTYSMR components was sealed in a bag. The mass ratio between CCFT–CCTYSMR and AC was calculated using $C_+ \times m_+ = C_- \times m_- \times \Delta V_-$, where m_-, ΔV_-, and C_- reveal the mass, voltage window, and capacitance of AC. Besides, m_+ and C_+ display the mass and capacity of the CCFT–CCTYSMR. In the AC||CCFT–CCTYSMR, the masses of CCFT–CCTYSMR and AC were 4 mg and 31.9 mg, respectively. The E_{den} and P_{den} of the AC||CCFT–CCTYSMR were computed using the equations.[6,7]

$$E_{den} = \frac{I \int V dt}{M \times 3.6} \quad (1)$$

$$P_{den} = \frac{E}{\Delta t} \times 3600 \quad (2)$$

3. Results and discussion

Our research presents a novel approach using a MOF to synthesize hierarchical CuCoFeTe–CuCoTe yolk-shelled microrods (CCFT–CCTYSMRs). This process involves several distinct conversion steps. Initially, MIL-88A microrods, a Fe-containing MOF, are converted into CoFeLDH–ZIF67 (CFLDH–ZIF67) through a reaction facilitated by Co^{2+} ions in the $C_4H_6N_2$ solution. This results in the evolution of the MIL-88A into CFLDH and the simultaneous self-assembly of ZIF67 nanocages around the core. The next stage involves an ion-exchange reaction with Cu^{2+} ions, transforming the ZIF layer into CCLDH nanocages that envelop internal CuCoFeLDH microrods, thus forming CuCoFeLDH–CuCoLDH yolk-shelled microrods. The final step is the tellurization, which results in the formation of CCFT–CCTYSMRs, noted for their outstanding supercapacitive performance (Fig. 1).

The morphological evolution during each synthesis stage is noticed through FESEM and TEM. The initial FESEM and TEM images disclose the MIL-88A sample as rod-like structures with a smooth surface and solid nature (Fig. S1, ESI†). The EDX of MIL-88A confirms the existence of C, O, and Fe elements in the sample (Fig. S2†). Post the self-assembly process, CFLDH–ZIF67 are completely covered by ZIF67 polyhedrons (Fig. 2a and b), with EDX pattern revealing a composition comprising C, N, O, Co, and Fe elements (Fig. S3†). Besides, the TEM image of the CFLDH–ZIF67 depicts the growth of ZIF67 particles on CFLDH solid rods (Fig. 2c). Subsequently, an ion-exchange reaction with Cu^{2+} ions results in CCFLDH–CCLDHYSMRs that preserve the rod-like architecture but exhibit a more intricate surface (Fig. 2d). A magnified image of a single CCFLDH–CCLDH particle (Fig. 2e) reveals that the surface comprises CuCoLDH particles. The EDX of the CCFLDH–CCLDH manifests signals of Cu, Fe, Co, C, and O (Fig. S4†). Also, the TEM image of the CCFLDH–CCLDH (Fig. 2f) illustrates the yolk–shell structure with an inner rod and a unique outer shell. Higher magnification indicates that the shell of CCFLDH–CCLDH consists of porous nanocages, with a 100 nm distance between the outer shell and the yolk surface (Fig. 2g). After undergoing tellurization, the CCFT–CCTYSMRs maintain their original morphology (Fig. 2h). The porous characteristics of the CCFT–CCTYSMRs are still discernible, verifying its hierarchical architecture (Fig. 2i). The EDX of the CCFT–CCTYSMR demonstrates elemental signals of Cu, Co, Te, and Fe in the sample, which illustrates the suc-

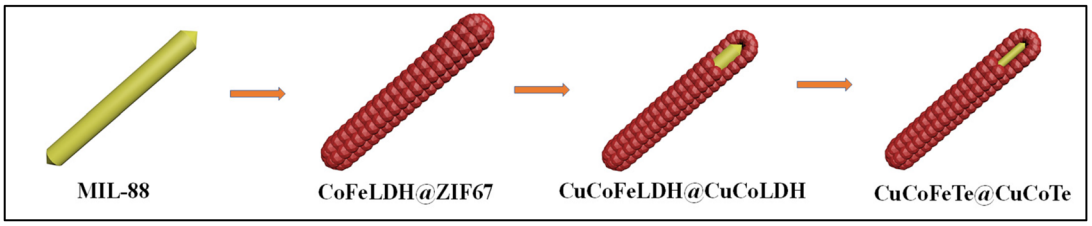

Fig. 1 Schematic illustration of the preparation process of the CCFT-CCTYSMR sample.

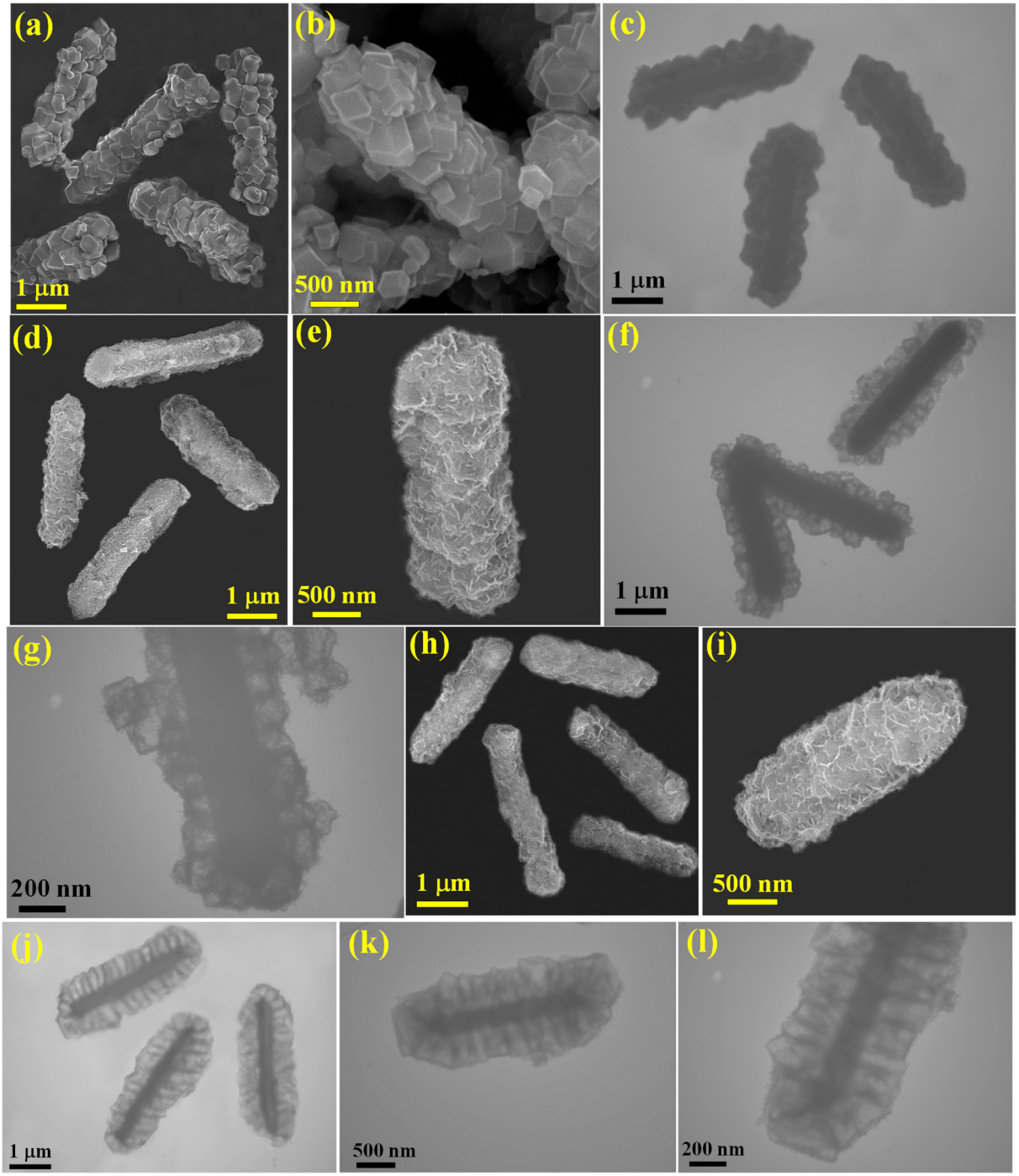

Fig. 2 (a and b) FESEM images of the CFLDH–ZIF67. (c) TEM image of the CFLDH–ZIF67. (d and e) FESEM images of the CCFLDH–CCLDHYSMR. (f and g) TEM images of the CCFLDH–CCLDHYSMR. (h and i) FESEM images of the CCFT–CCTYSMR. (j–l) TEM images of the CCFT–CCTYSMR.

cessful fabrication of CCFT–CCTYSMR (Fig. S5†). The FESEM mapping images (Fig. S6†) display the dispersion of Cu, Co, Te, and Fe within the CCFT–CCTYSMR sample. Also, the TEM image of the CCFT–CCTYSMR illustrates that the hollow nanocages are stably supported on rigid microrods (Fig. 2j), and magnified TEM images showcase each nanocage fabricated from interconnected CuCoTe nanoflakes (Fig. 2k and l). This exceptional architecture is expected to offer a multitude of active sites for the redox reactions, enhance the surface area for improved electrode/electrolyte interaction, and provide a buffering effect to enhance structural durability during charge–discharge cycles.[37,38]

The phase structure of our samples was analyzed through XRD as indicated in Fig. 3a and Fig. S7.† The XRD pattern of

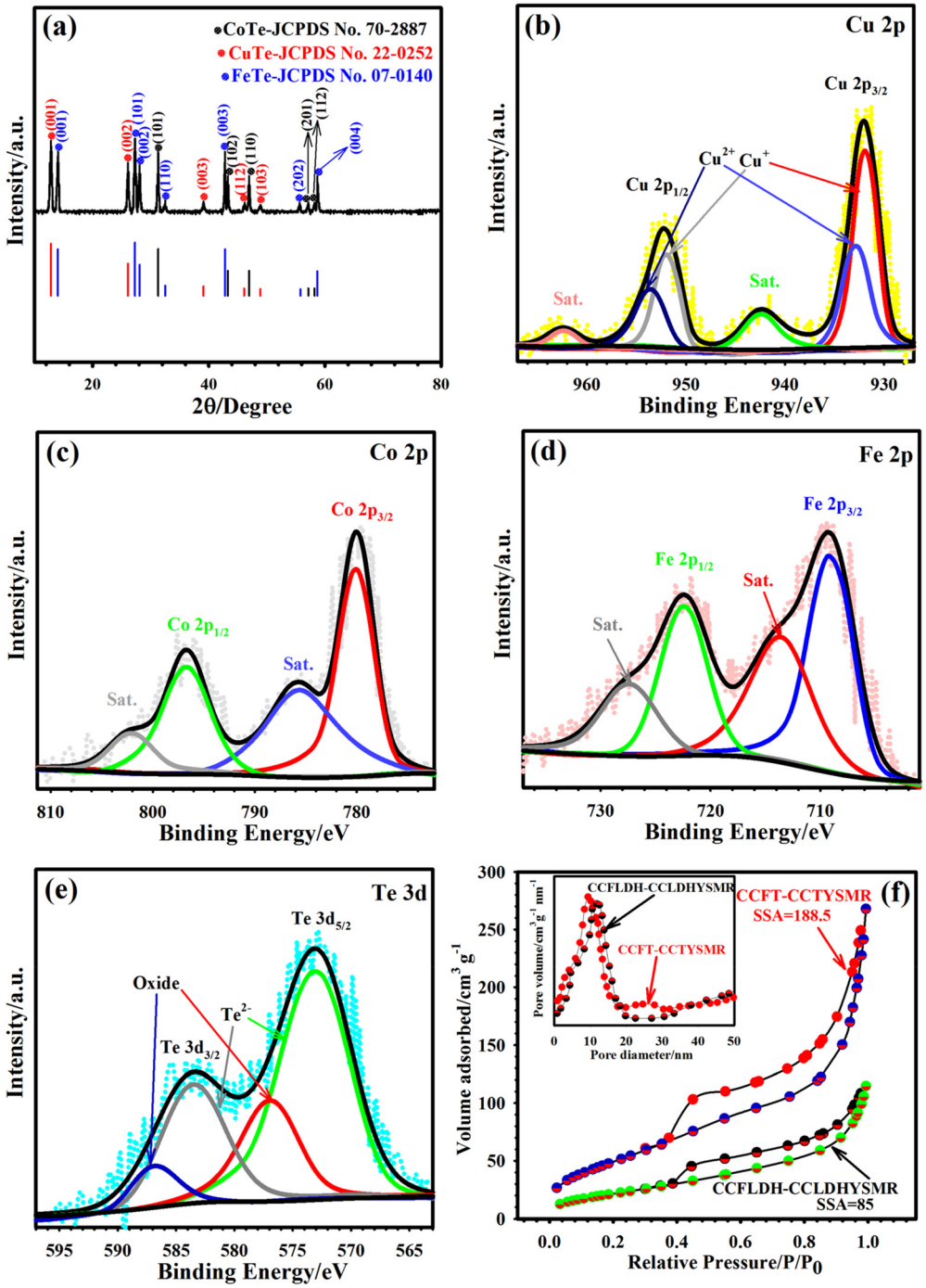

Fig. 3 (a) XRD of the CCFT–CCTYSMR. (b) Cu 2p XPS pattern of the CCFT–CCTYSMR. (c) Co 2p XPS pattern of the CCFT–CCTYSMR. (d) Fe 2p XPS pattern of the CCFT–CCTYSMR. (e) Te 3d XPS pattern of the CCFT–CCTYSMR. (f) BET curves of the CCFT–CCTYSMR and CCFLDH–CCLDHYSMR and their corresponding BJH curves (inset).

the MIL-88A sample confirms the crystallographic structure of MIL-88A (Fig. S7a†).[39] In the CFLDH–ZIF67, Co ion introduction into MIL-88A resulted in the complete disappearance of MIL-88A peaks, indicating the formation of LDH and ZIF67 phases (Fig. S7b†).[40,41] Subsequent ion-exchange with Cu^{2+} ions led to an XRD pattern characteristic of the typical LDH phase (Fig. S7c†).[42] For the CCFT–CCTYSMR sample, the XRD pattern reveals distinct peaks corresponding to CuTe, CoTe, and FeTe (Fig. 3a), aligning with JCPDS cards no. 22-0252, 70-2887, and 07-0140, respectively.[43–45] These include CuTe peaks at 12.85° (001), 26.10° (002), 39.10° (003), 46.12° (112), and, 48.90° (103), and CoTe peaks at 31.30° (101), 43.34° (102), 46.95° (110), 57.15° (201), and 58.22° (112). FeTe signals are observed at 14.03° (001), 27.30° (101), 28.10° (002), 32.50°

(110), 42.80° (003), 55.80° (202), and 58.70° (004). Furthermore, the XPS demonstrated the chemical states of Cu, Fe, Co, and Te in the CCFT–CCTYSMR structure. Fig. S8† displays the survey spectrum of the CCFT–CCTYSMR, which reveals the presence of Co, Cu, Fe, and Te in the sample. Notably, the O 1s peak is attributed to environmental O adsorption, while the C 1s peak stems from adventitious carbon due to material exposure.[46,47] Observing the detailed Cu 2p pattern in Fig. 3b, signals at 951.92 and 931.9 eV relate to the $2p_{1/2}$ and $2p_{3/2}$ peaks of Cu^{+}, while those at 953.23 and 932.92 eV correspond to the $2p_{1/2}$ and $2p_{3/2}$ peaks of Cu^{2+}.[48] Co 2p XPS pattern (Fig. 3c) reveals signals at 780.08 eV, 796.87 eV, and their satellite signals at 785.87 and 802.51, confirming Co^{2+} presence.[44,49] The Fe 2p pattern (Fig. 3d) features two signals at 708.92 and 722.33 eV for Fe^{2+}, along with satellite peaks at 713.81 and 727.41 eV.[50] Te 3d pattern in Fig. 3e presents noticeable peaks at 583.54 and 573.02 eV for Te^{2-} and signals at 576.92 and 586.93 eV likely indicating oxidation states of Te because of surface oxidation.[51] For supercapacitors, the specific surface area (SSA) and pore size are pivotal factors. To investigate these aspects for the CCFT–CCTYSMR and CCFLDH–CCLDHYSMR samples, N_2 adsorption and desorption tests were conducted. As seen in Fig. 3f, the adsorption–desorption isotherms for both materials reveal type IV characteristics with a conspicuous hysteresis loop, indicative of their mesoporous structure.[52–54] Notably, the SSA of the CCFT–CCTYSMR was estimated to be 188.5 $m^2\ g^{-1}$, which is higher than that of the CCFLDH–CCLDHYSMR (85 $m^2\ g^{-1}$). Further analysis of pore size distribution, carried out using the BJH (inset of Fig. 3f), confirms the mesoporous nature of both samples.[52–54] The BJH plots display peaks at approximately 9.35 nm for CCFT–CCTYSMR and 11.80 nm for CCFLDH–CCLDHYSMR. This mesoporosity is a crucial feature, as a large SSA combined with unique mesoporous properties significantly enhances ion and electron transport kinetics. These characteristics are essential in elevating the E_{den} and P_{den} and improving the longevity of supercapacitors.[15,17]

In assessing the energy storage behavior of our materials, a range of electrochemical tests, including CV, EIS, and GCD, were performed in a 6 M KOH. The selection of 6 M KOH, commonly utilized in supercapacitors for its excellent ionic conductivity and the small hydrated ionic radius of K^{+}, was informed by its optimal specific conductivity as demonstrated in previous studies.[55,56] Concentrations higher than 6 M were avoided to prevent material detachment from the NF.[55] The CV curves for CCFT–CCTYSMR, CCFLDH–CCLDHYSMR, CFLDH–ZIF67, MIL-88A, and pure NF at 10 mV s^{-1} are shown in Fig. 4a. The area under the curve for pure NF is significantly smaller with a weak current response in KOH electrolyte, highlighting its minimal contribution to energy storage. In contrast, the CCFT–CCTYSMR electrode demonstrates a considerably larger CV area and enhanced current response compared to the other electrodes, indicating superior capacity. This enhanced performance of the CCFT–CCTYSMR is attributed to increased conductivity due to the existence of the Te element and its high SSA. A higher SSA is beneficial for rapid electron kinetics and the creation of ample electroactive sites, thus yielding higher capacity values.[16,17] GCD plots for these electrodes at 1 A g^{-1} (Fig. 4b) further demonstrate the CCFT–CCTYSMR's superior charge storage performance. This might be ascribed to the synergistic effects of multiple metals, the unique yolk–shell architecture, and the incorporation of Te.[6,16,17] The specific capacity values of the prepared samples at 1 A g^{-1}, are illustrated in Fig. 4c. Here, the capacities of CCFT–CCTYSMR, CCFLDH–CCLDHYSMR, CFLDH–ZIF67, and MIL-88A are recorded as 1512, 812, 585.75, and 368 C g^{-1}, respectively. EIS experiments were conducted to investigate the conductivity and charge transfer kinetics of the samples. The Nyquist graphs, fitting the equivalent circuit of supercapacitors (inset of Fig. 4d), help determine the internal resistance (R_s) and charge-transfer resistance (R_{ct}). The R_s and R_{ct} for CCFT–CCTYSMR, measured as 0.10 and 0.15 Ω, respectively, are notably lower than those for CCFLDH–CCLDHYSMR (R_s = 0.21 Ω and R_{ct} = 0.26 Ω). This indicates enhanced electronic conductivity and favorable charge transfer kinetics in the CCFT–CCTYSMR, likely due to its distinctive morphology and the presence of tellurium ions.[16,17] Also, the CCFT–CCTYSMR exhibits the lowest diffusive resistance and fastest ion diffusion, as inferred from the slope of a straight line in its Nyquist plot.[16,17] Fig. 4e presents the CV curves of the CCFT–CCTYSMR from 10 to 50 mV s^{-1}, showing nearly identical shapes across all profiles. Oxidation and reduction peaks shift slightly with changing sweep rates, indicating excellent reversibility, good conductivity, and outstanding rate performance.[57] Besides, the CV curves for CCFLDH–CCLDHYSMR, CFLDH–ZIF67, and MIL-88A from 10 to 50 mV s^{-1} are revealed in Fig. S9.† The Faraday reactions for the CCFT–CCTYSMR electrode are:[58]

$$Cu/Co/FeTe + OH^- \leftrightarrow Cu/Co/FeTeOH + e^- \quad (3)$$

$$Cu/Co/FeTeOH + OH^- \leftrightarrow Cu/Co/FeTeO + H_2O + e^- \quad (4)$$

To delve deeper into the storage mechanism, we analyzed the association between current density and scanning speed using the equation $i_p = a\nu^b$, where 'a' and 'b' are coefficients, 'i' represents peak current density, and 'ν' is the sweep rate. Converting this to a logarithmic scale, $\log(i) = b\log(\nu) + \log(a)$, allows us to deduce the value of 'b' from the slope of $\log(i)$ *versus* $\log(\nu)$.[16,17] A 'b' value of 0.50 suggests a diffusion-controlled process, whilst a value of 1.0 indicates a capacitive process. As revealed in Fig. 4f, the linear fitting of peak current yields 'b' values of 0.5205 and 0.5244 for the reduction and oxidation peaks, respectively, signifying that the diffusion-controlled process predominantly governs the electrochemical reactions in our system.

To validate the superior electrochemical characteristics of the CCFT–CCTYSMR, we recorded GCD plots from 1 to 45 A g^{-1}. The CCFT–CCTYSMR electrode's GCD plots (Fig. 5a) showcased nonlinear charge and discharge curves with distinct plateaus, indicative of the battery-type behavior of the CCFT–CCTYSMR. The symmetric nature of these curves suggests high coulombic efficiency and good reversibility.[7,9] For com-

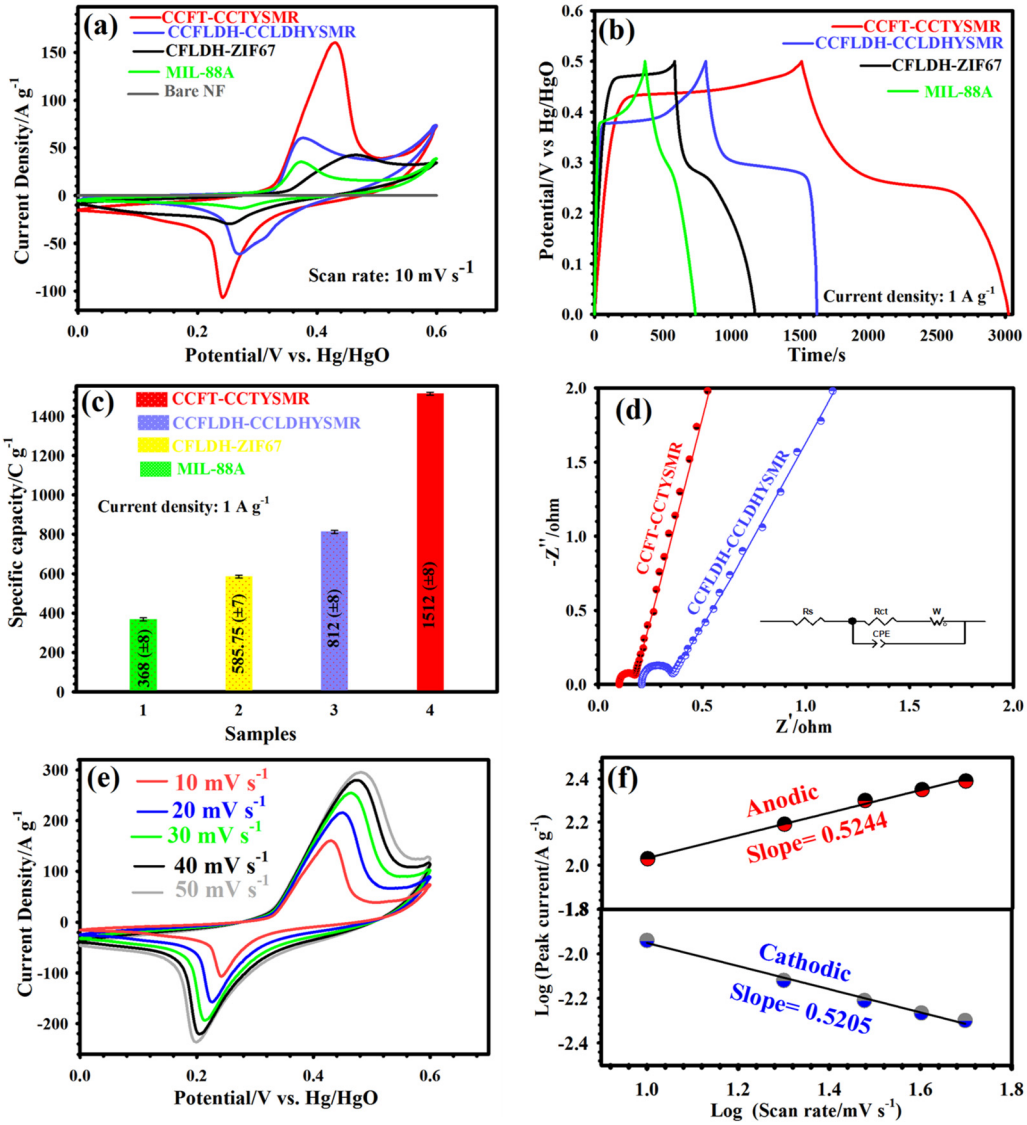

Fig. 4 Electrochemical tests of electrodes in a three-electrode system (all electrochemical tests were repeated three times). (a) CV curves of the CCFT–CCTYSMR, CCFLDH–CCLDHYSMR, CFLDH–ZIF67, MIL-88A, and pure NF electrodes at 10 mV s^{-1}. (b) GCD curves of the CCFT–CCTYSMR, CCFLDH–CCLDHYSMR, CFLDH–ZIF67, and MIL-88A electrodes at 1 A g^{-1}. (c) Specific capacities of the CCFT–CCTYSMR, CCFLDH–CCLDHYSMR, CFLDH–ZIF67, and MIL-88A electrodes at 1 A g^{-1} with the error bar. (d) Nyquist curves of the CCFT–CCTYSMR and CCFLDH–CCLDHYSMR electrodes (inset demonstrates the equivalent circuit model). (e) CV curves of the CCFT–CCTYSMR electrode from 10 to 50 mV s^{-1}. (f) Linear relation between the plot of the logarithm (I_p) *versus* logarithm (υ) of the CCFT–CCTYSMR.

parison, Fig. S10† highlights the GCD plots for MIL-88A, CFLDH–ZIF67, and CCFLDH–CCLDHYSMR. The capacity values of CCFT–CCTYSMR, along with CCFLDH–CCLDHYSMR, CFLDH–ZIF67, and MIL-88A, were estimated and are presented in Fig. 5b. The CCFT–CCTYSMR showed remarkable capacities of 1512, 1500.7, 1436, 1378.5, and 1276.5 C g^{-1} at 1, 2.5, 5, 25, and 45 A g^{-1}, respectively. These measurements significantly outperform the capacities of MIL-88A, CFLDH–ZIF67, and CCFLDH–CCLDHYSMR, which reached a maximum of only 368, 585.75, and 812 C g^{-1} at 1 A g^{-1}, respectively. Even at 45 A g^{-1}, the CCFT–CCTYSMR retained 84.45% of its original capacity, which is better than the retention rates for MIL-88A (35.4%), CFLDH–ZIF67 (52.8%), and CCFLDH–CCLDHYSMR (65.55%). The capacity of CCFT–CCTYSMR was compared with formerly reported samples, as reflected in Fig. 5c.[58–66] To assess the electrode materials' lifespan, continual GCD cycles were conducted for all electrodes at 25 A g^{-1}. The CCFT–CCTYSMR electrode impressively retained 91.86% of its initial capacity after 10 000 cycles (Fig. 5d), far exceeding the retention rates of MIL-88A (37.2%), CFLDH–ZIF67 (62%), and CCFLDH–CCLDHYSMR (78.5%) (Fig. S11†). Additionally, the CCFT–CCTYSMR maintained an excellent CE of 99.75% even after 10 000 cycles, manifesting exceptional reversibility (Fig. 5d). Post-longevity EIS profile (Fig. S12†) showed no significant change in R_s and R_{ct} values, demonstrating the material's remarkable durability.

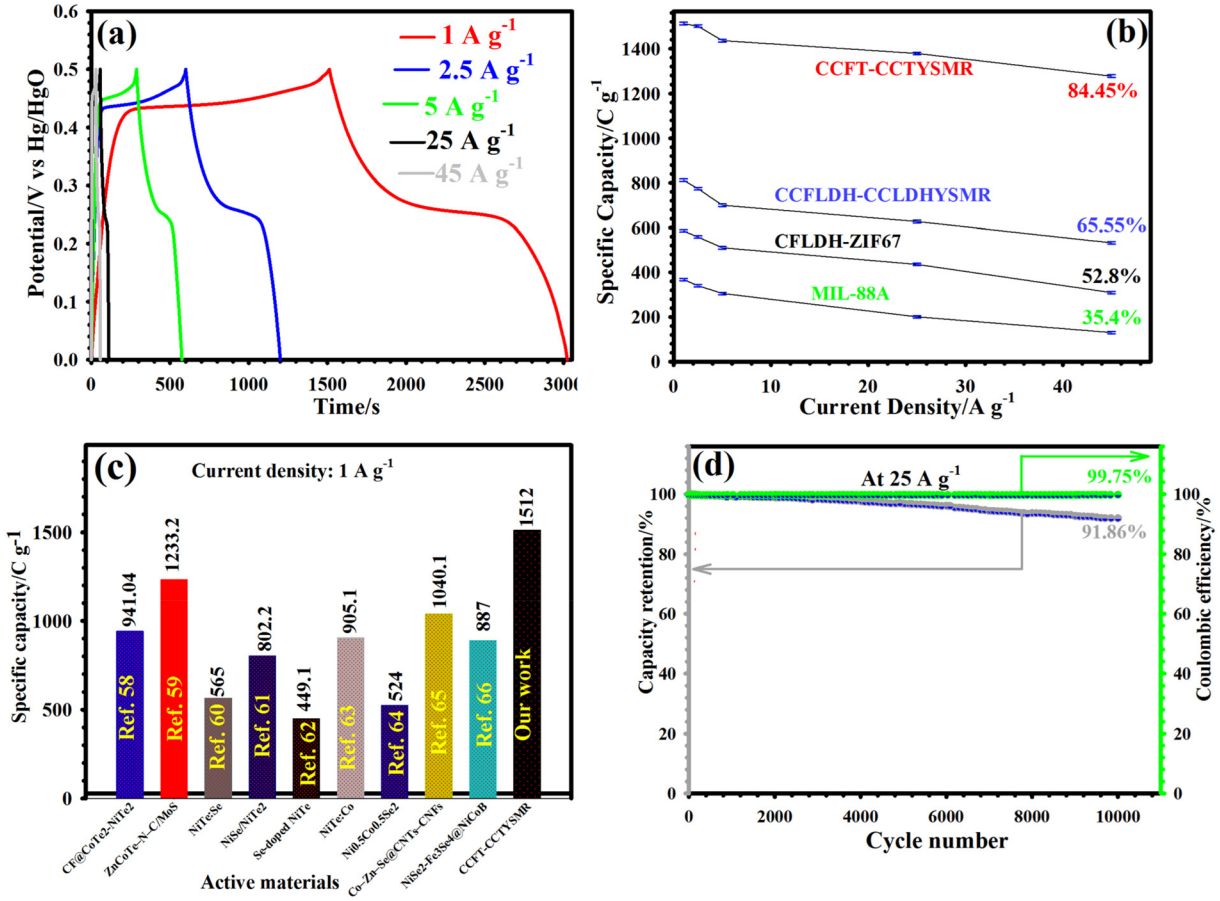

Fig. 5 (a) GCD graphs of the CCFT–CCTYSMR from 1 to 45 A g^{-1} (GCD tests were repeated three times). (b) Specific capacities *vs.* current densities of the CCFT–CCTYSMR, CCFLDH–CCLDHYSMR, CFLDH–ZIF67, and MIL-88A electrodes with the error bar. (c) Comparison of capacity of the CCFT–CCTYSMR at 1 A g^{-1} with the previous literature. (d) Longevity and coulombic efficiency of the CCFT–CCTYSMR at 25 A g^{-1}.

FESEM image of the cycled CCFT–CCTYSMR electrode confirmed the preservation of its morphology (Fig. S13†) and homogeneous dispersion of constituent elements (Cu, Te, Fe, and Co) (Fig. S14†). XRD analysis post 10 000 cycles (Fig. S15†) further verified the stability of the crystalline phase. The enhanced electrochemical features of the CCFT–CCTYSMR might be related to (i) the incorporation of Te species improving electrical conductivity and charge transfer;[16,17] (ii) the synergistic effect of Cu, Co, and Fe elements;[17,21] (iii) the unique yolk–shell structure with high porosity and large SSA ensuring structural integrity.[6] These factors contribute to CCFT–CCTYSMR's superior performance compared to other cathode electrodes, as detailed in Table S1.† Electrochemical experiments on the AC-based electrodes (Fig. S16†) also showed that AC exhibited quasi-rectangular CV profiles at 10 to 50 mV s^{-1} (Fig. S16a†) and nearly triangular GCD profiles at various current densities (Fig. S16b†), confirming its Electric Double-Layer Capacitor (EDLC) behavior. The estimated capacitances for the AC ranged from 189.50 to 143.75 F g^{-1} at current densities of 1 to 45 A g^{-1}, respectively (Fig. S16c†).

The exceptional electrochemical performance of the CCFT–CCTYSMR electrode prompted us to assess its utility in practical application. Therefore, we developed a hybrid device (AC||CCFT–CCTYSMR) using CCFT–CCTYSMR as a positive electrode and AC as a negative electrode, immersed in KOH. A detailed schematic of this hybrid device is presented in Fig. 6a. Based on the working potential windows determined for the CCFT–CCTYSMR (0 to 0.60 V) and AC (−1 to 0 V) in a three-electrode configuration (Fig. S17†), the voltage window of the AC||CCFT–CCTYSMR was set to a maximum of 1.6 V. The CV profiles recorded at various potential windows at 20 mV s^{-1} (Fig. S18†) indicated that extending the voltage window to 1.7 V led to polarization reactions in the CV curves, establishing 0–1.6 V as the optimal voltage range for the AC||CCFT–CCTYSMR. The CV curves of AC||CCFT–CCTYSMR within this voltage window, tested from 10 to 50 mV s^{-1} (Fig. 6b), demonstrated consistent shapes, signifying an excellent rate capability. This consistency, even at higher sweep speeds, highlighted the successful combination of EDLC and battery-like properties in the hybrid device. The GCD curves for the AC||CCFT–CCTYSMR from 1 to 45 A g^{-1} (Fig. 6c) were nearly symmetric, showcasing efficient and rapid charge storage processes with high coulombic efficiency. The device's capacities, detailed in Fig. 6d, were registered as 285.60,

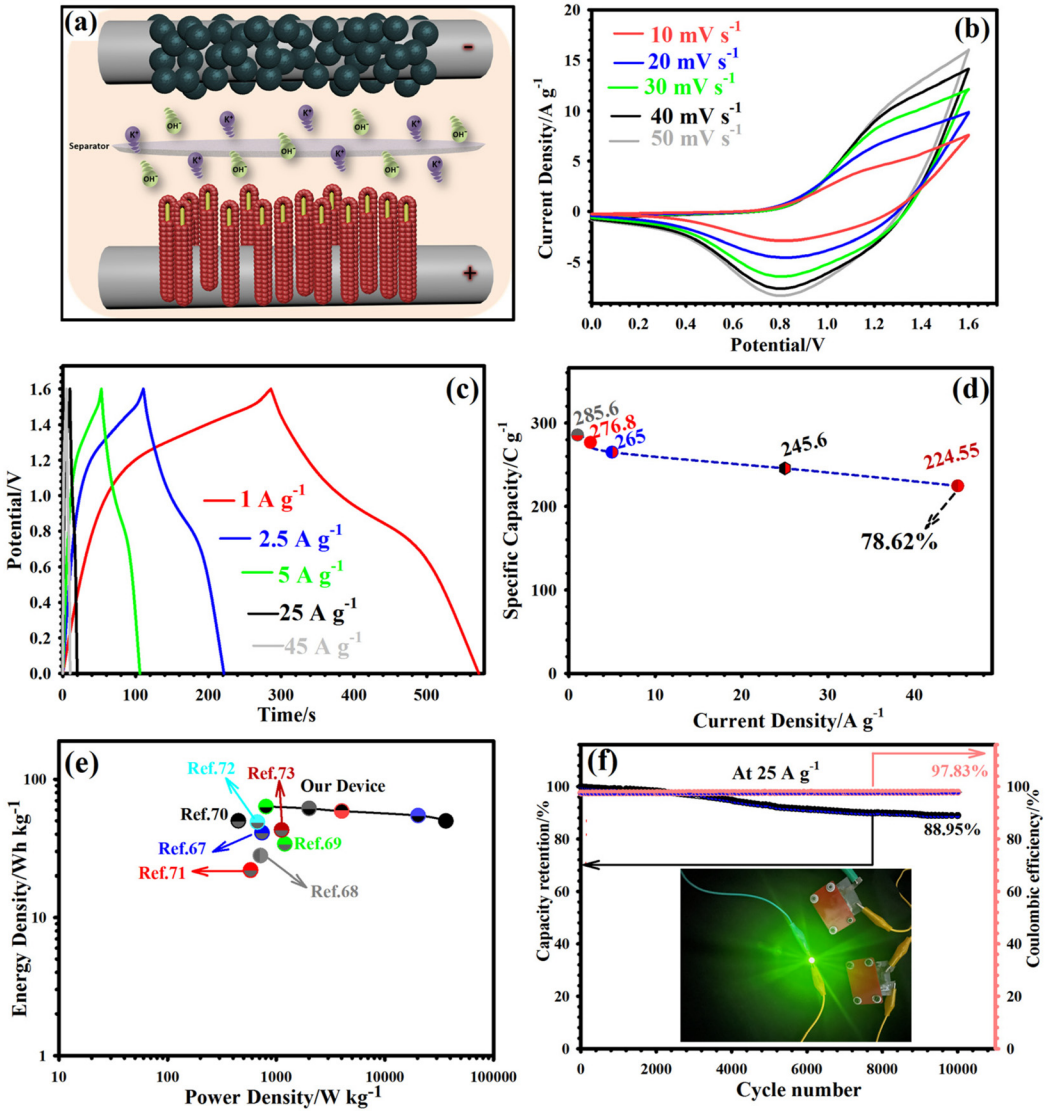

Fig. 6 Electrochemical tests of the AC||CCFT–CCTYSMR device (all electrochemical tests were repeated three times). (a) Schematic illustration of the AC||CCFT–CCTYSMR. (b) CVs of the AC||CCFT–CCTYSMR from 10 to 50 mV s^{-1}. (c) GCD graphs of the AC||CCFT–CCTYSMR from 1 to 45 A g^{-1}. (d) Specific capacity *vs.* current density of the AC||CCFT–CCTYSMR. (e) The comparison of the AC||CCFT–CCTYSMR device's Ragone graph with several devices. (f) Durability and coulombic efficiency of the AC||CCFT–CCTYSMR at 25 A g^{-1} (the inset shows the photograph of a green LED with two AC||CCFT–CCTYSMR devices).

276.80, 265, 245.60, and 224.55 C g^{-1} at 1, 2.5, 5, 25, and 45 A g^{-1}, respectively. A Ragone plot (Fig. 6e) revealed the E_{den} and P_{den} of the AC||CCFT–CCTYSMR. The AC||CCFT–CCTYSMR delivered a maximum E_{den} of 63.46 W h kg^{-1} under a P_{den} of 803.80 W kg^{-1} and maintained an E_{den} of 49.90 W h kg^{-1} under a P_{den} of 36 423.35 W kg^{-1}, demonstrating its potential for diverse applications. As indicated in Fig. 6e, the values of energy densities of the AC||CCFT–CCTYSMR are better than several devices.[67–73] The cycling durability and CE of our device were evaluated through repeated charging and discharging at 25 A g^{-1}. From Fig. 6f, it is evident that the AC||CCFT–CCTYSMR maintained as much as 88.95% of its original capacity even after 10 000 cycles, while its CE stood at 97.83% over the same number of cycles. This performance not only indicates remarkable electrochemical stability and reversibility but also highlights the device's endurance. To demonstrate its practical application, two AC||CCFT–CCTYSMR devices were connected in series and successfully powered a green LED, as shown in Fig. 6f (inset). Our research not only introduces a promising cathode material for hybrid supercapacitors but also inspires material design for a range of applications.

4. Conclusions

This study introduces an advanced conversion methodology for synthesizing CuCoFeTe–CuCoTe yolk-shelled microrods (CCFT–CCTYSMRs), a novel and efficient electrode material

designed for hybrid supercapacitors. Our investigation demonstrates the superior electrochemical performance of the CCFT–CCTYSMR in comparison to the CCFLDH–CCLDHYSMR, particularly in aspects of specific capacity, rate capability, and cycling stability. The exceptional supercapacitive behavior of the CCFT–CCTYSMR can be assigned to its peculiar yolk-shelled structure, the synergistic combination of Cu, Fe, and Co elements, and the inclusion of highly conductive Te. Leveraging the remarkable capabilities of the CCFT–CCTYSMR, we successfully assembled a high-performance AC||CCFT–CCTYSMR hybrid device, employing CCFT–CCTYSMR as a positive electrode and AC as a negative electrode. This device showcased a high capacity of 285.60 C g^{-1} and an impressive E_{den} of 63.46 W h kg^{-1} at 803.80 W kg^{-1}, accompanied by an outstanding electrochemical stability of 88.95%. The development and successful fabrication of the CCFT–CCTYSMR highlight an effective approach in designing innovative electrode materials, paving the way for the advancement of next-generation energy storage devices.

Conflicts of interest

The authors declare no competing financial interest.

Acknowledgements

The authors gratefully acknowledge the support of this work by Research councils of Shahid Beheshti University.

References

1 C. Wang, S. Zhao, X. Song, N. Wang, H. Peng, J. Su, S. Zeng, X. Xu and J. Yang, *Adv. Energy Mater.*, 2022, **12**, 2200157.
2 X. Guan, X. Fan, E. Zhu, J. Zhang, L. Yang, P. Yin, X. Guan and G. Wang, *J. Colloid Interface Sci.*, 2024, **658**, 952–965.
3 Z. Zhai, W. Yan, L. Dong, J. Wang, C. Chen, J. Lian, X. Wang, D. Xia and J. Zhang, *Nano Energy*, 2020, **78**, 105193.
4 L. Yang, J. Lu, E. Zhu, J. Zhang, X. Guan, B. Liu, P. Yin and G. Wang, *Appl. Surf. Sci.*, 2024, **645**, 158847.
5 L. Yang, E. Zhu, W. Zhang, X. Guan, B. Liu, P. Yin and G. Wang, *J. Alloys Compd.*, 2024, **973**, 172878.
6 B. Ameri, A. Mohammadi Zardkhoshoui and S. S. Hosseiny Davarani, *Mater. Chem. Front.*, 2021, **5**, 4725–4738.
7 A. Mohammadi Zardkhoshoui, B. Ameri and S. S. Hosseiny Davarani, *Chem. Eng. J.*, 2023, **470**, 144132.
8 X. Guan, J. Chen, E. Zhu, P. Yin, L. Yang, X. Guan and G. Wang, *J. Mater. Sci. Technol.*, 2023, **150**, 145–158.
9 A. Mohammadi Zardkhoshoui and S. S. Hosseiny Davarani, *Sustainable Energy Fuels*, 2021, **5**, 900–913.
10 X. Zhou, Y. Ren, Y. Lu, Z. Cheng, W. Wang, Q. Wang, W. Huang and X. Dong, *Adv. Mater. Interfaces*, 2019, **6**, 1901138.
11 L. Wang, R. Zhang, Y. Jiang, H. Tian, Y. Tan, K. Zhu, Z. Yu and W. Li, *Nanoscale*, 2019, **11**, 13894–13902.
12 K. Song, W. Li, J. Xin, Y. Zheng, X. Chen, R. Yang, W. Lv and Q. Li, *Chem. Eng. J.*, 2021, **419**, 129435.
13 J. Zhang, Y. Deng, Y. Wu, Z. Xiao, X. Liu, Z. Li, R. Bu, Q. Zhang, W. Sun and L. Wang, *Chem. Eng. J.*, 2022, **430**, 132836.
14 A. Mohammadi Zardkhoshoui, M. Maleka Ashtiani, M. Sarparast and S. S. Hosseiny Davarani, *J. Power Sources*, 2020, **450**, 227691–227699.
15 M. Amiri, A. Mohammadi Zardkhoshoui, S. S. Hosseiny Davarani, M. Maghsoudi and M. K. Altafi, *Sustainable Energy Fuels*, 2022, **6**, 3626–3642.
16 M. Molaei, G. Rahmati Rostami, A. Mohammadi Zardkhoshoui and S. S. Hosseiny Davarani, *J. Colloid Interface Sci.*, 2024, **653**, 1683–1693.
17 D. Dehghanpour Farashah, F. Beigloo, A. Mohammadi Zardkhoshoui and S. S. Hosseiny Davarani, *Chem. Eng. J.*, 2023, **474**, 145584.
18 A. Mohammadi Zardkhoshoui, R. Hayati Monjoghtapeh and S. S. Hosseiny Davarani, *Energy Fuels*, 2020, **34**, 14934–14947.
19 A. Mohammadi Zardkhoshoui, S. S. Hosseiny Davarani, M. Maleka Ashtiani and M. Sarparast, *J. Mater. Chem. A*, 2019, **7**, 10282–10292.
20 Z. Ji, K. Liu, W. Dai, D. Ma, H. Zhang, X. Shen, G. Zhu and S. Wu, *Nanoscale*, 2021, **13**, 1689–1695.
21 A. Mohammadi Zardkhoshoui and S. S. Hosseiny Davarani, *Chem. Eng. J.*, 2020, **402**, 126241–126252.
22 Y. Chen, J. Yang, H. Yu, J. Zeng, G. Li, B. Chang, C. Wu, X. Guo, G. Chen, L. Zheng and X. Wang, *ACS Appl. Energy Mater.*, 2022, **5**, 6772–6782.
23 A. Mohammadi Zardkhoshoui and S. S. Hosseiny Davarani, *Nanoscale*, 2020, **12**, 1643–1656.
24 A. Mohammadi Zardkhoshoui, B. Ameri and S. S. Hosseiny Davarani, *Chem. Eng. J.*, 2022, **435**, 135170.
25 D. Gao, R. Liu, D. Han, P. Xu, P. Wang and Y. Wei, *J. Mater. Chem. A*, 2023, **11**, 9546–9554.
26 Z. Yu, S. Jiao, J. Tu, Y. Luo, W.-L. Song, H. Jiao, M. Wang, H. Chen and D. Fang, *ACS Nano*, 2020, **14**, 3469–3476.
27 D. Dehghanpour Farashah, F. Beigloo, A. Mohammadi Zardkhoshoui and S. S. Hosseiny Davarani, *Sustainable Energy Fuels*, 2023, **7**, 4922–4934.
28 Y. Qi, Z. Yang, S. Peng, Y. Dong, M. Wang, X.-Q. Bao, H. Li and D. Xiong, *Inorg. Chem. Front.*, 2022, **9**, 332–342.
29 Y.-C. Chen, Y.-G. Lin, Y.-K. Hsu, S.-C. Yen, K.-H. Chen and L.-C. Chen, *Small*, 2014, **10**, 3803–3810.
30 Z. Andikaey, A. A. Ensafi and B. Rezaei, *Electrochim. Acta*, 2021, **393**, 139061.
31 A. Mohammadi Zardkhoshoui and S. S. Hosseiny Davarani, *Nanoscale*, 2020, **12**, 12476–12489.
32 S. Kim, J. Lauterbach and E. Sasmaz, *ACS Catal.*, 2021, **11**, 8247–8260.
33 L.-S. Lin, J. Song, H.-H. Yang and X. Chen, *Adv. Mater.*, 2018, **30**, 1704639.

34 H. Mei, L. Zhang, K. Zhang, J. Gao, H. Zhang, Z. Huang, B. Xu and D. Sun, *Electrochim. Acta*, 2020, **357**, 136866.
35 Z. Ma, R. Zheng, Y. Liu, Y. Ying and W. Shi, *J. Colloid Interface Sci.*, 2021, **602**, 627–635.
36 H. Chen, J. Zhou, Q. Li, S. Zhao, X. Yu, K. Tao, Y. Hu and L. Han, *Dalton Trans.*, 2020, **49**, 10535–10544.
37 M. Amiri, A. Mohammadi Zardkhoshoui and S. S. Hosseiny Davarani, *Nanoscale*, 2023, **15**, 2806–2819.
38 B. Ameri, A. Mohammadi Zardkhoshoui and S. S. Hosseiny Davarani, Sustainable, *Energy Fuels*, 2020, **4**, 5144–5155.
39 S. S. E. Ghodsinia, H. Eshghi and A. Mohammadinezhad, *Sci. Rep.*, 2023, **13**, 8092.
40 X. Qiao, H. Kang, J. Wu, Y. Li, Q. Wang, X. Jia, Y. Qiao, S. Lu, X. Wu and W. Qin, *Int. J. Hydrogen Energy*, 2019, **44**, 31987–31994.
41 M. Wang, J. Liu, C. Guo, X. Gao, C. Gong, Y. Wang, B. Liu, X. Li, G. G. Gurzadyan and L. Sun, *J. Mater. Chem. A*, 2018, **6**, 4768–4775.
42 S. Zhou, C. Li, G. Zhao, L. Liu, J. Yu, X. Jiang and F. Jiao, *J. Mater. Sci.: Mater. Electron.*, 2019, **30**, 19009–19019.
43 J. U. Salmón-Gamboa, A. H. Barajas-Aguilar, L. I. Ruiz-Ortega, A. M. Garay-Tapia and S. J. Jiménez-Sandoval, *Sci. Rep.*, 2018, **8**, 8093.
44 L. Zhang, J. Liang, L. Yue, K. Dong, Z. Xu, T. Li, Q. Liu, Y. Luo, Y. Liu, S. Gao, A. M. Asiri, Q. Kong, X. Guo and X. Sun, *J. Mater. Chem. A*, 2021, **9**, 21703–21707.
45 M. Cheng, X. Zhao, Y. Zeng, P. Wang, Y. Wang, T. Wang, S. J. Pennycook, J. He and J. Shi, *ACS Nano*, 2021, **15**, 19089–19097.
46 J. Li, J. Zhao, R. Tang, Q. Chen, Z. Niu, M. Li, C. Guo, J. Su and L. Zhang, *J. Power Sources*, 2020, **449**, 227517–227523.
47 S. C. Sekhar, B. Ramulu, D. Narsimulu, S. J. Arbaz and J. S. Yu, *Small*, 2020, **16**, 2003983.
48 S. Kumaravel, K. Karthick, P. Thiruvengetam, J. M. Johny, S. S. Sankar and S. Kundu, *Inorg. Chem.*, 2020, **59**, 11129–11141.
49 S. Huang, S. Li, Q. He, H. An, L. Xiao and L. Hou, *Appl. Surf. Sci.*, 2019, **476**, 769–777.
50 N. Jayababu, S. Jo, Y. Kim and D. Kim, *ACS Appl. Mater. Interfaces*, 2021, **13**, 19938–19949.
51 S. Zhang, L. Qiu, Y. Zheng, Q. Shi, T. Zhou, V. Sencadas, Y. Xu, S. Zhang, L. Zhang, C. Zhang, C.-L. Zhang, S.-H. Yu and Z. Guo, *Adv. Funct. Mater.*, 2021, **31**, 2006425.
52 A. Mohammadi Zardkhoshoui, B. Ameri and S. S. Hosseiny Davarani, *Nanoscale*, 2021, **13**, 2931–2945.
53 A. Mohammadi Zardkhoshoui and S. S. Hosseiny Davarani, *Dalton Trans.*, 2020, **49**, 10028–10041.
54 B. Ameri, A. Mohammadi Zardkhoshoui and S. S. Hosseiny Davarani, *Dalton Trans.*, 2021, **50**, 8372–8384.
55 W. Jiang, F. Hu, Q. Yan and X. Wu, *Inorg. Chem. Front.*, 2017, **4**, 1642–1648.
56 R. J. Gilliam, J. W. Graydon, D. W. Kirk and S. J. Thorpe, *Int. J. Hydrogen Energy*, 2007, **32**, 359–364.
57 H. Guo, A. Zhang, H. Fu, H. Zong, F. Jin, K. Zhao and J. Liu, *Chem. Eng. J.*, 2023, **453**, 139633.
58 C. Shi, Q. Yang, S. Chen, Y. Xue, Y. Hao and Y. Yan, *ACS Appl. Energy Mater.*, 2022, **5**, 2817–2825.
59 M. B. Poudel, A. R. Kim, S. Ramakrishan, N. Logeshwaran, S. K. Ramasamy, H. J. Kim and D. J. Yoo, *Composites, Part B*, 2022, **247**, 110339.
60 S. Deshagani, P. Ghosal and M. Deepa, *Electrochim. Acta*, 2020, **345**, 136200.
61 J. Liu, L. Ren, J. Luo and J. Song, *Colloids Surf., A*, 2022, **647**, 129093.
62 B. Ye, M. Huang, S. Jiang, L. Fan, J. Lin and J. Wu, *Mater. Chem. Phys.*, 2018, **211**, 389–398.
63 B. Ye, M. Huang, L. Fan, J. Lin and J. Wu, *J. Alloys Compd.*, 2019, **776**, 993–1001.
64 X. Song, C. Huang, Y. Qin, H. Li and H. C. Chen, *J. Mater. Chem. A*, 2018, **6**, 16205–16212.
65 L.-P. Lv, C. Zhi, Y. Gao, X. Yin, Y. Hu, D. Crespy and Y. Wang, *Nanoscale*, 2019, **11**, 13996–14009.
66 Z. Tian, K. Zhou, M. Xie, Y. Zhang, J. Chen, C. Du and L. Wan, *Chem. Eng. J.*, 2022, **447**, 137495.
67 M. S. Vidhya, R. Yuvakkumar, G. Ravi, A. G. Al-Sehemi, V.-H. Nguyen and D. Velauthapillai, *Energy Fuels*, 2022, **36**, 1726–1734.
68 S. Lalwani, S. Karade, J.-H. Eum and H. Kim, *ACS Appl. Energy Mater.*, 2021, **4**, 2430–2439.
69 Z. Xie, D. Qiu, J. Xia, J. Wei, M. Li, F. Wang and R. Yang, *ACS Appl. Mater. Interfaces*, 2021, **13**, 12006–12015.
70 H. Dan, K. Tao, Y. Hai, L. Liu and Y. Gong, *Nanoscale*, 2019, **11**, 16810–16827.
71 S. M. Dinara, A. K. Samantara, J. K. Das, J. N. Behera, S. K. Nayak, D. J. Late and C. S. Rout, *Dalton Trans.*, 2019, **48**, 16873–16881.
72 Y. Zhao, S. Wang, F. Ye, W. Liu, J. Lian, G. Li, H. Wang, L. Hu and L. Wu, *J. Mater. Chem. A*, 2022, **10**, 16212–16223.
73 T. Kshetri, T. I. Singh, Y. S. Lee, D. D. Khumujam, N. H. Kim and J. H. Lee, *Composites, Part B*, 2021, **211**, 108624.